Soft Matter

PAPER

View Article Online
View Journal | View Issue

Cite this: *Soft Matter*, 2025, **21**, 9100

Received 27th June 2025,
Accepted 16th October 2025

DOI: 10.1039/d5sm00671f

rsc.li/soft-matter-journal

Controlling topological textures of umbilics using spatiotemporal magnetic fields

Nina Kravets,* Gregorio Gonzalez-Cortes and Etienne Brasselet

The generation, evolution and manipulation of topological defects in thin films of liquid crystals is a long-standing subject of study in the soft matter sciences, but one that is still relevant today. Here we report control over the generation of textures of umbilic defects in electrically biased nematic liquid crystals using a spatiotemporally structured magnetic field. This is exemplified by exploiting the symmetries of the magnetic field generated by an array of four permanent magnets for the reconfigurable generation of textures with central umbilics with topological charge ±1. The experimental observations are qualitatively supported by evaluating the orientational response of the liquid crystal to the magnetic torque density from the exact determination of the 3D magnetic field. Furthermore, we derive a 2D amplitude equation from the Frank–Oseen free energy, which allows the quantitative description and prediction of the morphogenesis of different liquid crystal topological textures. This spatiotemporal approach shows how symmetry-guided field-orientation coupling enables deterministic control of topological defects, offering new routes for structuring anisotropic soft materials.

1. Introduction

The role played by the symmetries of external fields interacting with matter is especially pronounced when using soft matter, and in particular in liquid crystals, for which non-local orientational behavior can give rise to a multitude of self-organization processes, often accompanied by the emergence of topological defects. As ordered fluids, the spatiotemporal state of liquid crystalline mesophases is usually described by the director field, represented by the unit vector $\vec{n}(\vec{r},t)$, which indicates the local average orientation of the anisotropic building blocks constituting the material. In nonpolar nematic liquid crystals (nematics), as is the case in this work, the director is a headless quantity ($\vec{n} \equiv -\vec{n}$).[1] Nematics can exhibit topological defects, which are defined as locations in space (*e.g.*, points, lines or loops) where at least one attribute of $\vec{n}$ is undefined. In addition, topological defects can be either nonsingular or singular, depending on whether the director remains defined or not.[2,3] Defects can emerge from spontaneous or induced symmetry breaking under the action of external fields of various nature (*e.g.*, electrical, magnetic, optical, thermal, mechanical), and their structure and dynamics are deeply influenced by the geometry and boundary conditions of the system.

Here, in the context of thin nematic slabs confined between two parallel substrates provided with strong perpendicular (homeotropic) orientational boundary conditions, we focus our attention on a particular kind of liquid crystal topological defects known as umbilics.[4] Umbilics are nonsingular bulk director structures that spontaneously appear when using nematics with negative dielectric anisotropy and applying a sufficiently strong quasistatic electric field $\vec{E}$ oriented along the direction given by the director at rest, $\vec{n}_0$ orthogonal to confining substrates (Fig. 1a). Indeed, electrically induced reorientation to a given $\theta(x,y,z) \neq 0$ takes place above the electric Fréedericksz threshold which corresponds to a voltage[1] $V_\mathrm{F} = \sqrt{\dfrac{K_3\pi^2}{\varepsilon_0|\varepsilon_\mathrm{a}|}}$, where K_3 is bend Frank elastic constant and ε_a is the dielectric anisotropy of the nematic.[5] The initial azimuthal degeneracy of the field-matter system leads to spontaneous symmetry breaking and the subsequent emergence of umbilic defects. Umbilics are locally described by azimuthally varying projection of the director field on the plane of the sample, $\vec{n}_\perp$, whose orientation angle ψ (Fig. 1a) is given by $\psi = m\phi + \psi_0$, where ϕ is the angular polar coordinate in the plane (x,y), ψ_0 is a constant, and m is the topological charge. Although arbitrary integer values of m satisfy the continuity of the director field, one only observes umbilics with $m = \pm 1$ as high charge umbilics ($|m| > 1$) are unstable.[4] The 3D director field around $m = \pm 1$ umbilics is depicted with streamlines in Fig. 1(b–e). Since the initial unperturbed orientational state $\vec{n}_0$ is translation-invariant in the plane (x,y), a random distribution of umbilics with $m = \pm 1$ appears for $V > V_\mathrm{F}$. Their spatiotemporal evolution is dictated by long-range elastic interactions

---

Université de Bordeaux, CNRS, Laboratoire Ondes et Matière d'Aquitaine, F-33400, Talence, France. E-mail: nina.kravets@u-bordeaux.fr

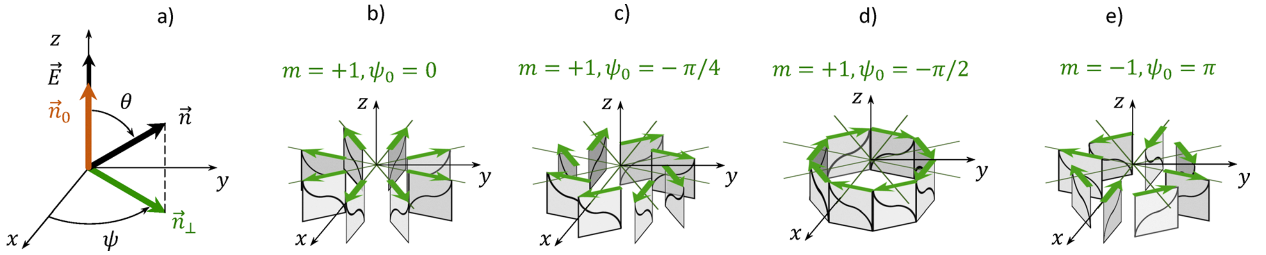

Fig. 1 (a) Definition of the main vectors and angles. (b–e) Sketches of 3D structure of umbilics with $m = \pm 1$ and different ψ_0. For each meridional cross-section oriented at an angle ϕ from 0 to 2π by step of $\pi/4$, the black solid line indicates the streamline of $\vec{n}$ and the green arrow indicates its projection $\vec{n}_\perp$ on the (x,y) plane.

that eventually lead to their disappearance *via* the annihilation of oppositely-charged umbilics.[6] As such, the study and use of umbilics require the development of methods to stabilize them, ideally in space and time.

So far, several strategies have been developed to control the position of a single or arrays of umbilics, for instance, using thermally induced convection,[7] electrically induced convection,[8–10] optical reorientation,[11] photo-electric reorientation,[12,13] patterned electric reorientation,[14,15] reorientation *via* the topography of the confining surface,[16] magneto-electric reorientation,[17–21] or electro-acoustic reorientation.[22] It is worth noting that, the spatially controlled generation of isolated umbilics with $m = -1$ is usually a byproduct of the generation of umbilics with $m = +1$. More rarely, it is a direct consequence of a nonaxisymmetric 3D structured torque density applied to the director field. An example of this was reported by Pieranski *et al.*[19] by means of a judicious 3D configuration of four permanent magnets whose resulting magnetic field lines correspond, in a finite region of space, to the director field of an umbilic with $m = -1$ over millimeter-size spatial extent. An electrical analog was demonstrated a few years later by You *et al.*[15] over a spatial extent of a few tens of microns. By design, the latter approach enables periodic arrays of defects to be generated reproducibly but prevents post-fabrication spatial reconfiguration and comes with limited overall tunability of the reorientation amplitude.

Here we report on how the spatial and spatio-temporal characteristics of a magnetic field, in conjunction with the application of a uniform electric field, can be used to generate umbilics in a controlled and reconfigurable manner both in terms of spatial location and topological charge. In Section 2, we recall how a magnetic field, when combined with the use of a uniform electric field, can provide control over the position of the generated umbilics. In Section 3, we introduce a circular array of four magnets and demonstrate experimentally that its symmetry features can be used to control the sign of the topological charge of the central umbilic in the generated orientational texture. We also provide a qualitative discussion of the observations based on the knowledge of the 3D magnetic field. In Section 4, we present a parametric study of the morphogenesis of orientational textures as a function of the asymmetry of the magnetic array. We derive a 2D amplitude equation from the Frank–Oseen free energy density variation and compare experimental observations with a quantitative numerical study. This is further extended in Section 5 to the use of spatiotemporally structured magnetic fields, for which time brings an extra degree of freedom to generate and manipulate assemblies of defects that would be difficult to obtain otherwise. Finally, our concluding remarks are collected in Section 6.

2. Magnetoelectric generation of defect textures

Magnetic fields are widely used to orient soft matter systems spanning from colloids to biological objects.[23] In particular, magnetic fields are a powerful tool for aligning liquid crystals when strategies based on alignment layers[24] or the electrodes[25] are not applicable. Most nematics possess positive anisotropy of the diamagnetic permeability, meaning that the director tends to align parallel to the magnetic field direction. Given the relatively low diamagnetic anisotropy of nematic, a uniform electric field is often applied in addition to the magnetic field in order to reinforce its effect.

As a background, we consider three specific situations in which electric and magnetic fields give rise to generic director textures—umbilics and walls—that are pivotal to the present study. We then introduce the nematic sample and the magnets used in our experiments followed by a description of how the director field was experimentally retrieved *via* optical polarimetry measurements.

We used a 19 μm-thick nematic film sandwiched between 1 mm-thick glass plates covered with transparent ITO electrodes and a surface alignment layer providing homeotropic anchoring. The chosen nematic (MRLC-01 from Beam, USA) has wide temperature range −40 °C to 101 °C, negative dielectric anisotropy $\varepsilon_a = -6.4$ at 1 kHz and 25 °C, and positive diamagnetic anisotropy χ_a (not measured). We applied a 2 kHz square-wave AC voltage whose root-mean-square amplitude was 3% to 5% higher than the measured threshold value, $V_F = 1.8\ V_{RMS}$. The resulting director fields were studied using polarization microscopy. All provided experimental images were recorded in transmission mode between crossed linear polarizers whose orientation is indicated by P (polarizer) and A (analyzer) in the figures. The signs of the experimentally observed topological charges were confirmed using spatially resolved Stokes polarimetry. For this, the nematic sample was illuminated with right-handed circularly polarized light. The spatially resolved transmitted intensity $I_\alpha(x,y)$ was measured in four images projected with a linear polarizer whose orientation was set at an angle α = 0°, 45°, 90° and 135° with respect to the x axis. The reconstructed director azimuth was calculated as $\tilde{\psi}(x,y) = \frac{1}{2}\arctan\left(\frac{I_{45} - I_{135}}{I_0 - I_{90}}\right) + \frac{\pi}{4}$ and unwrapped into $\psi \in [0, 2\pi]$ when needed. Indeed, although the only knowledge of $\tilde{\psi}$ is sufficient to identify the sign of m, it lacks the information about out-of-plane orientation necessary for the 3D assessment of $\vec{n}$, noting that $\vec{n}_\perp \neq -\vec{n}_\perp$. The equivalence between the information encoded in the 3D unitary headless vector $\vec{n}$ defined by (θ,ψ) and the 2D polar vector $\vec{n}$ defined by $(|\vec{n}_\perp|, \psi)$ is ensured by assigning the initial orientation $\vec{n}_0 = \vec{e}_z = (0,0,1)$ and projecting the reoriented $\vec{n}$ onto the (x,y) plane, as sketched in Fig. 1(a). By doing so, the azimuth and sign of $\vec{n}$ are encoded in the direction of $\vec{n}_\perp$ characterized by ψ, while the voltage-dependent angle θ is encoded in $|\vec{n}_\perp|$. Following this convention, we can univocally represent the 3D structure of an umbilic by a 2D vector field as illustrated in Fig. 1(b–e), in which we adopted the graphical presentation of Pieranski *et al.*[19]

As mentioned previously, applying uniform electric field alone leads to the formation of a numerous randomly positioned umbilics with topological charge $m = \pm 1$ seeded by thermal noise and sample imperfections (see Fig. 2a). In contrast, other textures can be generated by breaking the initial symmetry,[26] for instance, by applying a magnetic field prior to the electric field. We illustrate this by placing permanent neodymium (grade N42) magnets on the surface of the nematic sample. For example, in Fig. 2(b) we demonstrate an inversion wall known as Néel wall[18,19] which we created using a curved magnetic field whose in-plane projection $\vec{B}_\perp = \begin{pmatrix} B_x \\ B_y \end{pmatrix}$ maintains a uniform orientation, while its vertical component B_z reverses its sign, similar to the experiment reported by Gilli *et al.*[18] The resulting $\vec{n}_\perp$ follows the sign-inversion of B_z, which leads to the creation of two domains with π-shifted in-plane director orientation ψ aligned with the direction of $\vec{B}_\perp$. This illustrates the importance of the z component of the 3D magnetic field for the formation of director textures. Another example is shown in Fig. 2(c), where a permanent disk or ring magnet with uniform magnetization along the z-axis generates an axisymmetric magnetic field distribution around the z, closely resembling that of the 3D director field of $m = +1$ umbilic, see Fig. 1(b), which leads to the formation and trapping of a single $m = +1$ umbilic around the axis of the magnet. It is worth noting the naturally swirled structure of the resulting umbilic.[27] It is related to the splay elastic constant larger than the twist elastic constant for most nematic liquid crystals. Indeed, the latter favors a twist configuration of the director (as in Fig. 1d) near the umbilic core, where the director gradients are the largest, despite the splay configuration (as in Fig. 1b) inherently imposed by the magnetic realignment action. These two distinct configurations are connected with topology-preserving continuous in-plane rotation of $\vec{n}_\perp$ when as the umbilic core is approached, with ψ_0 varying smoothly from 0 to $\pm\pi/2$, as sequentially depicted in Fig. 1(b–d).

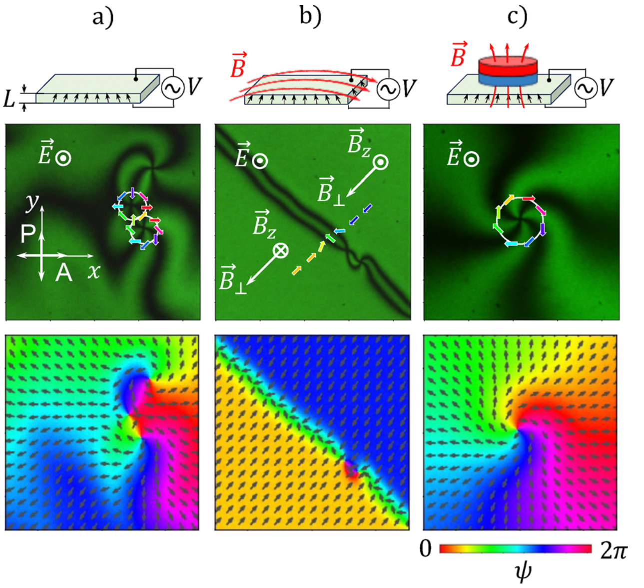

Fig. 2 Cross-polarized microscope images (top) and corresponding director maps reconstructed using spatially resolved Stokes polarimetry (bottom). (a) Spatially uniform electric field alone providing a random distribution of umbilics. (b) Spatially uniform electric field in combination with uni-directionally curved magnetic field provides formation of a Néel wall with defects. (c) An axisymmetric magnetic field combined with spatially uniform electric field provides formation of a single $m = +1$ umbilic. The field of view in each panel is 3 mm × 3 mm.

3. Controlling topological charge of umbilics

3.1. Qualitative perturbative approach

We propose controlling the generation of umbilics with prescribed topological charge by using structured magnetic fields tailored to the symmetry of their 3D director configurations. We demonstrate this using a simple circular array of four permanent magnets with alternating polarity and achieve control over the sign of topological charge by introducing a slight spatiotemporal asymmetry into the array.

The magnetic configuration consists of four permanent cylindrical magnets with diameter d = 3 mm and height h = 1.5 mm. The center of the array is positionned at (0,0,0), while the centers of magnets with the same polarity are separated by distances a and b as shown in Fig. 3(a). In the present study, a and b are adjustable parameters, provided that the magnets remain in contact with their immediate neighbors in all configurations. The nematic slab is placed below the magnet's surface at $z_0 = -h/2 - \tilde{z}_0$ where $\tilde{z}_0$ = 1 mm denotes the vertical offset between the lower facet of the magnets and the upper facet of the nematic slab. The resulting magnetic configuration exhibits a hyperbolic-like topological charge $m = -1$ in $\vec{B}_\perp(x, y, z_0)$ centered at the $(x, y) = (0,0)$, illustrated by the streamlines in Fig. 3(b) while red and blue colors indicate the amplitude of B_z.

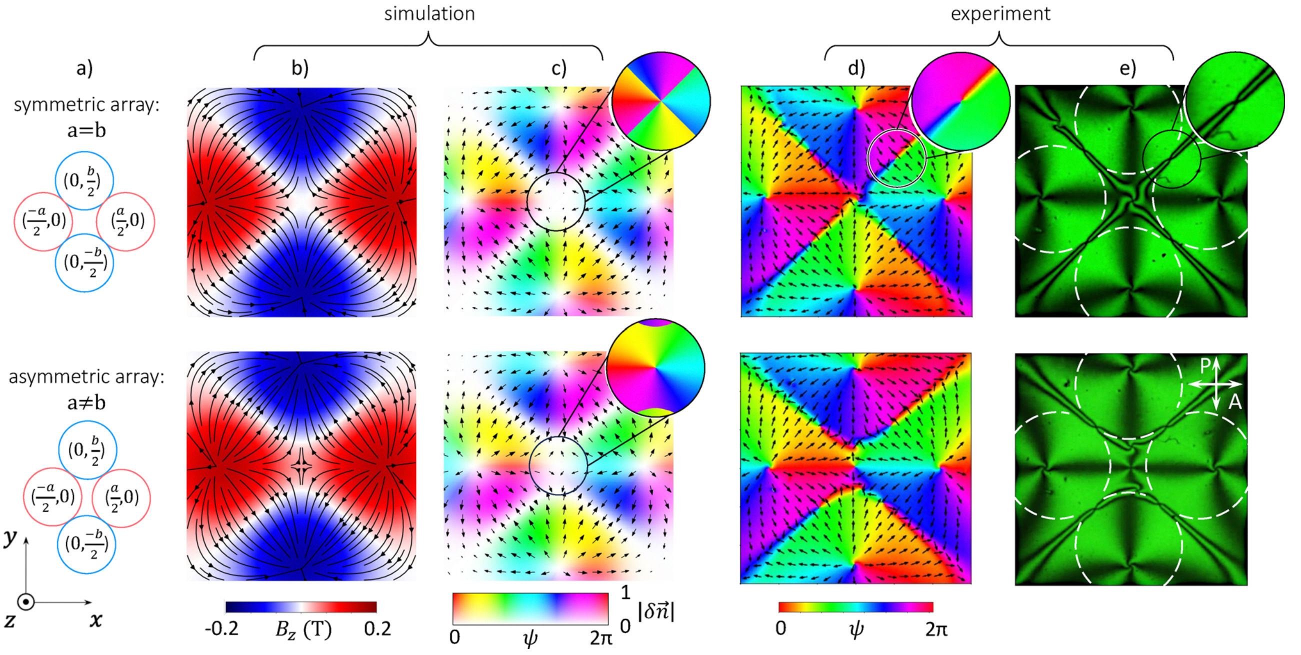

Fig. 3 Experimental results for symmetric (a = b) and asymmetric (b = 1.2a) arrays of magnets generating textures featuring central umbilics with topological charges m = +1 and m = −1, respectively. (a) Sketch of the magnet array configuration. (b) Calculated resulting magnetic field components B_z (color) and $\vec{B}_\perp$ (streamline). (c) Calculated normalized amplitude (saturation) and azimuth (hue and arrows) of $\delta\vec{n}$. The zoom to the central area shows the phase of $\delta\vec{n}$ with the amplitude information discarded. (d) Experimentally observed orientation of the in-plane director field $\vec{n}_\perp$ reconstructed using spatially resolved Stokes polarimetry (hue and arrows). (e) Corresponding cross polarized microscope image: polarizer (P) and analyzer (A) are oriented along y- and x-axes, respectively. The zoom to the selected area in (d) and (e) highlights the m = −1 umbilic hosted on one of the Néel walls. The field of view in panels (b–e) is 6 mm× 6 mm.

To predict the topology of the texture that can be seeded by the magnetic field, we qualitatively evaluate the director field distortions from the unperturbed state in a perturbative manner as,

$$\delta\vec{n} \propto \vec{\Gamma} \times \vec{n}_0 \propto B_z \begin{pmatrix} B_x \\ B_y \\ 0 \end{pmatrix}. \tag{1}$$

Here, $\vec{\Gamma} \propto \left(\vec{n}_0 \cdot \vec{B}\right)\left(\vec{n}_0 \times \vec{B}\right)$ is the magnetic torque exerted on $\vec{n}_0$. We show calculated $\delta\vec{n}$ maps in Fig. 3(c). The amplitude of $\delta\vec{n}$ reaches maximum under individual magnets, but vanishes along vertical lines passing near their centers, as well as along the vertical planes passing between the neighboring magnets. This corresponds to the seeding of four m = +1 umbilics separated by director walls where $\delta\vec{n}$ reverses its direction. Near the center, B_z—and hence $\vec{\Gamma}$ and $\delta\vec{n}$—vanish. Around the center, the phase of $\delta\vec{n}$ experiences four π−jumps (see zoomed area in the Fig. 3c). This discontinuous $\delta\vec{n}$ map does not correspond to the seeding of either to m = +1 nor to m = −1 umbilic.

To obtain an unambiguous connection between the perturbed director $\vec{n} \approx \vec{n}_0 + \delta\vec{n}$ and the 3D structure of an umbilic, we introduce a small asymmetry in the position of the magnets in the array (here we consider $a < b$, but the same reasoning applies to $a > b$). This creates a central region around $(0, 0, z_0)$ of non-zero sign-invariant B_z component. In this configuration, the magnetic aligning effect manifests itself directly in the continuous $\delta\vec{n}$ map corresponding to a seed of m = −1 umbilic located between two inversion walls close to the center of the array (see zoomed area in the Fig. 3c). This analysis is confronted to the experiment in what follows.

3.2. Experimental confirmation

In Fig. 3(d and e) we present experimentally observed director maps corresponding to the described magnetic field configurations with a = b and $a < b$. The white dashed circles in Fig. 3(e) indicate the areas covered by the magnets, which were briefly removed to acquire the cross-polarized images and the $I_\alpha(x,y)$ maps necessary for reconstructing $\vec{n}_\perp(x, y)$. We confirm the formation of four m = +1 umbilic defects under each magnet. However, the structure of the inversion walls and the central topological textures warrant a more detailed discussion.

In the symmetric case (a = b), the central texture is that of a single m = +1 umbilic located at the intersection of two Néel walls hosting four m = −1 umbilic defects (see zoomed area in the Fig. 3(d and e). In the asymmetric case ($a \neq b$), an m = −1 umbilic is located near the origin between two non-crossing curved Néel walls hosting four m = −1 umbilics and two additional m = +1 umbilics. As a matter of fact, these textures cannot be explained by magnetically-induced seed alone. Their morphogenesis requires a refined treatment accounting for elastic energy minimization in the presence of electric field-induced reorientation.

Still, the magnetic seeding qualitative approach remains valuable. While the director distortion induced by the structured

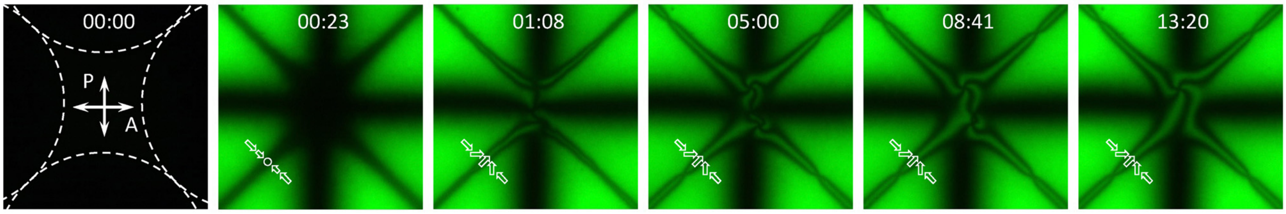

Fig. 4 Formation of transient textures in nematic slab seeded by the structured magnetic field obtained from a slightly asymmetric (b = 1.05a) magnetic array and grown by the application of a uniform electric field. Each cross-polarized microscope image shows a 6 mm × 6 mm field of view. The timestamps are given in mm:ss format. The white arrows illustrate local Ising-like and Néel-like distributions of in-plane director orientation.

magnetic field alone is hardly detectable in the present experimental configuration (see the dark image in Fig. 4), its influence becomes evident in the early stages of the reorientation dynamics triggered by the combination of magnetic and electric fields. As illustrated in Fig. 4, the initial formation of crossing Ising-like walls reflects a seeded director configuration, in line with the behavior expected from the magnetic seeding approach. As the reorientation progresses, these Ising-type walls transform into Néel-type walls, a process favored by the anisotropic elastic constants of the nematic. This transformation is accompanied by the nucleation of umbilic defects, consistent with the expected defect-mediated texture evolution.[18]

At later times, the texture is strongly influenced by the spatial symmetry of the four-magnet configuration. In the asymmetric case, a central negative umbilic is robustly seeded and revealed upon electric field application. In contrast, a near-symmetric configuration leads to further evolution of the texture *via* elastic interactions between nearby umbilics, which can drive annihilation events[28,29] and ultimately result in a single positive central umbilic. The signature of the asymmetry remains visible as a slight off-centered position of the central m = +1 umbilic. Although the final states may depart from perturbative predictions, the transient regime observed experimentally for b = 1.05a (see Fig. 4)) confirms that magnetic seeding provides a robust and insightful qualitative framework.

4 Morphogenesis of magnetically tailored topological textures

4.1 Spatiotemporal 2D amplitude equation

The dynamics of the liquid crystal director reorientation under the action of external magnetic and electric fields in presence of strong anchoring can be described by introducing the total free energy $F=\int f\,\mathrm{d}V$, where $f = f_\mathrm{e} + f_\mathrm{E} + f_\mathrm{B}$ is the free energy density, where

$$f_\mathrm{e}=\frac{K_1}{2}\left(\vec{\nabla}\cdot\vec{n}\right)^2+\frac{K_2}{2}\left(\vec{n}\cdot\left(\vec{\nabla}\times\vec{n}\right)\right)^2+\frac{K_3}{2}\left(\vec{n}\times\left(\vec{\nabla}\times\vec{n}\right)\right)^2, \tag{2}$$

$$f_\mathrm{E}=-\frac{\varepsilon_0\varepsilon_\mathrm{a}}{2}\left(\vec{E}\cdot\vec{n}\right)^2, \tag{3}$$

$$f_\mathrm{B}=-\frac{\chi_\mathrm{a}}{2\mu_0}\left(\vec{B}\cdot\vec{n}\right)^2, \tag{4}$$

correspond to the elastic, electric, and magnetic free energy densities, respectively. The elastic distortions characterized by splay, twist and bend Frank elastic constants K_1, K_2 and K_3 dominate the coarsening of the liquid crystal texture.[6,30] The electric field $\vec{E}=(0,0,E)$ drives the creation of umbilics through global director reorientation. In contrast, the magnetic field $\vec{B}=(B_x,\ B_y,\ B_z)$ only induces inhomogeneous, perturbative director reorientation $(\chi_\mathrm{a}(B_x{}^2 + B_y{}^2 - B_z{}^2) \ll -\varepsilon_0\mu_0\varepsilon_\mathrm{a}E^2)$, which is further reinforced by electrical means.

To describe the dynamics of the director field we introduce the dissipation density function R in the absence of velocity field as $R=\frac{\gamma}{2}\frac{\partial\vec{n}}{\partial t}\cdot\frac{\partial\vec{n}}{\partial t}$, where γ is the rotational viscosity coefficient. Then, applying the variational principle while preserving $\vec{n}\cdot\vec{n}=1$,[1] the director dynamics is described by

$$\gamma\frac{\partial\vec{n}}{\partial t}=-\frac{\partial f}{\partial\vec{n}}+\vec{n}\left(\vec{n}\cdot\frac{\partial f}{\partial\vec{n}}\right). \tag{5}$$

Close to the Fréedericksz transition, the deviations of the director with respect to the z axis are small, allowing the 3D director field to be approximated by retaining only the fundamental longitudinal mode:

$$\vec{n}(x,y,z)\approx\begin{pmatrix} X(x,y)\sin(\pi(z-z_0+L)/L) \\ Y(x,y)\sin(\pi(z-z_0+L)/L) \\ 1-\dfrac{X(x,y)^2+Y(x,y)^2}{2}\sin^2(\pi(z-z_0+L)/L) \end{pmatrix} \tag{6}$$

where X and Y are the director amplitudes along the x- and y-directions, respectively, and L is the thickness of the nematic slab. By substituting the ansatz (6) into eqn (5), and performing the following rescaling of time, spatial coordinates, and director amplitudes:

$$\frac{\pi^2K_3}{\gamma L^2}t\to t, \tag{7}$$

$$\frac{\pi}{L}\sqrt{\frac{2K_3}{(K_1+K_2)}}(x,y)\to(x,y), \tag{8}$$

$$\left(\frac{3}{4}\frac{V^2}{V_\mathrm{F}{}^2}+2\frac{K_1}{K_3}-3\right)^{-\frac{1}{2}}(X,Y)\to(X,Y), \tag{9}$$

and integrating along the z-coordinate, we derive a Ginzburg–

Landau-like amplitude equation:[31,32]

$$\frac{\partial}{\partial t}\begin{pmatrix} X \\ Y \end{pmatrix} = \left(\mu - X^2 - Y^2 + \nabla_\perp^2 + 2\delta\frac{\partial^2}{\partial x \partial y}\sigma_x - \delta\left(\frac{\partial^2}{\partial x^2} - \frac{\partial^2}{\partial y^2}\right)\sigma_z\right) \times \begin{pmatrix} X \\ Y \end{pmatrix} + \beta B_z \vec{B}_\perp + \sqrt{I}\begin{pmatrix} \xi_X \\ \xi_Y \end{pmatrix}. \quad (10)$$

Here $\mu = \left(\frac{V^2}{{V_F}^2} - 1\right)$ is the linear bifurcation parameter, $\delta = \frac{K_1 - K_2}{K_1 + K_2}$ is the dimensionless splay-twist elastic anisotropy of the liquid crystal, and σ_x and σ_z are the conventional Pauli matrices. The parameter $\beta = \frac{L^2 \chi_a}{\pi^2 \mu_0 K_3}\sqrt{\left(\frac{3}{4}\frac{V^2}{{V_F}^2} + 2\frac{K_1}{K_3} - 3\right)}$ quantifies the strength of interaction between the liquid crystal and the magnetic field while accounting for the presence of a uniform electric field. Finally, accounting for thermal fluctuations inherent to the experiments, we introduce small orientational fluctuations in the director orientation by adding Gaussian white noise distributions $\xi_X(x,y,t)$ and $\xi_Y(x,y,t)$, each with zero mean, intensity $\sqrt{I}$ and spatiotemporal correlations $\langle \xi_i(x,y,t)\xi_j(x',y',t')\rangle = \delta(x,x')\delta(y,y')\delta(t,t')\delta(i,j)$. These stochastic fluctuations significantly impact the director orientation only where $\left|\beta B_z \vec{B}_\perp\right| < \sqrt{I}$ and when $V < V_F$. When $V < V_F$, the spatial distribution of $B_z \vec{B}_\perp$ drives the reorientation of the liquid crystal, biasing the position where umbilics are generated. When $V > V_F$, the stationary texture results from the competition between the magnetic, electric and elastic torque densities.

Eqn (10) allows the calculation of the director field under experimental-like conditions, given four parameters: μ, δ, β, and I. We solve eqn (10) numerically by discretizing space with a regular uniform square stencil of 512 points per dimension, using a forward Euler method with a time step of 0.1 time units and imposing natural boundary conditions. For our study, we set $\mu = 0.5$, $I = 10^{-10}$ and $\delta = 0.3$. The chosen μ value, slightly higher that in the experiment, optimizes the computational cost with no expected physical consequences. The positive values of δ reflect the typical anisotropy of most available nematics. Notably, the effect of $\delta > 0$ manifests itself through the swirling of umbilic arms[27] as discussed in the introduction. For the numerical simulations we have explored values of β between 1 T^{-2} and 100 T^{-2}, given typical values of χ_a of the order of 10^{-6}.

Regarding the spatial distribution of the magnetic field, in the present study we model the arrays of magnets using exact solutions for magnetized cylinders,[33–35] thereby going beyond the commonly used far-field approximations.[19,21] This allows to resolve detailed shape of individual magnets located close to the liquid crystal cell.

4.2. Parametric phase map of topological textures

In order to quantitatively assess the asymmetry of the magnet configurations, from the purely symmetric ($a = b$) to the most asymmetric situation ($a = d$, $b = \sqrt{3}d$), we introduce the static (st) asymmetry parameter $A_{\rm st} = \frac{(\sqrt{3}+1)^2}{2}\frac{|b-a|}{b+a}$. By construction, $0 \leq A_{\rm st} \leq 1$ with $A_{\rm st} = 1$ corresponding to a pair of magnets of identical polarity being in contact. In the experiments, the accessible range of $A_{\rm st}$ goes up to $A_{\rm st} = 0.78$ due to strong magnetic repulsion between magnets of the same polarity.

From a numerical parametric investigation in the ($A_{\rm st}$,β) parameter plane, we have identified six distinct orientational textures, labeled from (*i*) to (*vi*), as shown in Fig. 5(a) and (b). Four of the observed textures are associated with well-defined assemblies of umbilics. In our analysis, we choose to classify the states according to the sign and position of the central umbilic, as well as the number of umbilics confined to the adjacent walls. When describing the states, we emphasize these specific characteristics, deliberately omitting a complete listing of all umbilics visible in the figures. For each pair of values ($A_{\rm st}$,β), the numerical protocol consists of first computing the magnetically induced orientational seed at $\mu = -1$, followed by computing the final director texture resulting from the combined action of magnetic and electric fields at $\mu = 0.5$.

At low β, the seeding action of the magnetic field is too weak, allowing the coarsening process to yield a quasihomogeneous texture denoted as *i*). As β increases, each magnet traps a $m = +1$ umbilic near its center, while $m = -1$ umbilics are generated in the regions between adjacent magnets. We notice the transient formation of a single $m = +1$ umbilic in the center of the magnet array. Yet, the magnetic potential landscape is not pronounced enough to keep the central $m = +1$ umbilic permanently and the latter annihilates with one of the neighboring $m = -1$ defects. The final texture containing four $m = +1$ umbilics and three $m = -1$ umbilics is identified as *ii*) in Fig. 5. At higher values of β, several routes unfold depending on the asymmetry parameter $A_{\rm st}$. At low $A_{\rm st}$ a single $m = +1$ umbilic gets permanently trapped in the center of the array (singlet state *iii*) in Fig. 5. As $A_{\rm st}$ increases, the position of the central umbilic undergoes a spontaneous symmetry breaking along the *y*-axis *via* a continuous transition (off-centered singlet state *iv*) in Fig. 5. As the asymmetry increases, an umbilic triplet—one $m = -1$ umbilic in the center and two $m = +1$ umbilics on the walls above and below—is trapped instead of a singlet, (state *v*) in Fig. 5. Further increase of $A_{\rm st}$ reduces the curvature of the Néel walls, enabling the annihilation of the pairs umbilics trapped on the wall (state *vi*) in Fig. 5. Last but not least, the chosen requirement to keep neighboring magnets in contact implies that the spatial structure of the magnetic potential landscape in the center of the array may become too fine to be spatially resolved by the liquid crystal, as the elastic interactions tends to eliminate energy-costly short-range gradients of the director field. As a result, for a wide range of $A_{\rm st}$ and β, the central umbilic disappears *via* annihilation with one of the neighboring umbilics, and higher values of β are required to change from the state (*ii*) to one of the states with stable central umbilic.

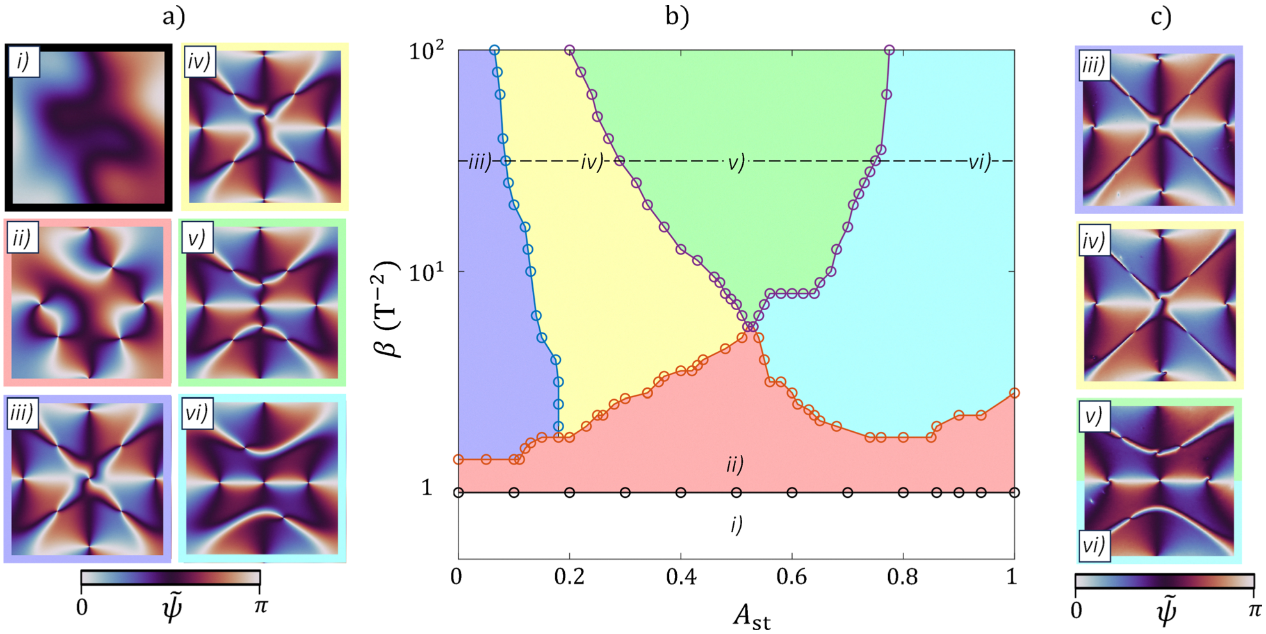

Fig. 5 Numerically simulated and experimentally observed topological textures for static structured magnetic fields provided by the magnet configurations illustrated in Fig. 3(a). The cyclic color map represents the in-plane director orientation $\tilde{\psi}$. (a) Numerically simulated (from eqn (10)) textures illustrating unique features of these orientational states: *i)* quasihomogeneous texture at A_{st} = 0.4, β = 0.5 T^{-2}, *ii)* Four m = +1 umbilics trapped under each magnet and quasihomogeneous central part at A_{st} = 0.14, β = 3.1 T^{-2}, *iii)* An m = +1 umbilic trapped in the center of the magnet array at A_{st} = 0.10, β = 31.5 T^{-2}, *iv)* Off-centered m = +1 umbilic at A_{st} = 0.32, β = 31.5 T^{-2}, *v)* Central m = −1 umbilic at A_{st} = 0.48, β = 31.5 T^{-2}, *vi)* Central m = −1 umbilic and annihilation of umbilic pairs trapped at the wall at A_{st} = 0.9, β = 31.5 T^{-2}. (b) Diagram of the distinctive states numerically identified by varying A_{st} and β. The horizontal dashed line refers to a value of $\beta \approx 30$ T^{-2} that corresponds to our estimation for a typical experiment. (c) Experimentally reconstructed director azimuth maps $\tilde{\psi}(x,y)$ at A_{st} = 0.03, 0.12, and 0.78, respectively. The experimental $\tilde{\psi}(x,y)$ maps were obtained following the protocol described in the Section 2 of this paper. The field of view in each panel is 6 mm × 6 mm.

Since the experimental setup provides relatively strong magnetic seeding (the roughly estimated value of β corresponding to a typical experiment is indicated as a dashed line in Fig. 5) we were able to observe centered (*iii*) and off-centered (*iv*) singlet states, as well as triplet states. In contrast to numerics, the non-ideality of the experiments leads to the observation of hybrid director states, in which one of Néel walls contains a single $m = -1$ umbilic (state *vi*), while the other Néel wall contains two $m = -1$ umbilics separated by one $m = +1$ umbilic (state *v*).

5. Spatiotemporally structured magnetic fields

5.1. Time-averaging approach

So far, we have considered the control of topological textures relying on spatial symmetry breaking imposed by the structure of driving fields. Here, we propose to exploit the temporal degree of freedom as a means to induce and shape spatial symmetry breaking. This approach relies on the fact that the director's response to a time-varying driving field becomes overdamped at high frequencies due to the viscous nature of liquid crystals. It is well established, for instance in display technologies, that nematic slabs are driven by high-frequency (typically, kHz or higher) ac electric fields, which generate an effective torque density governed by the RMS value of the field while suppressing ion migration.[36] Similarly, the liquid crystal responds to the time-averaged magnetic torque, provided that the magnetic field varies rapidly enough for the system to be in the overdamped dynamic regime.[17]

By imposing an appropriate time-variation of the magnetic field, one can generate a wide variety of torque textures, including configurations that are unachievable through static structuring of permanent magnets. For simplicity, we restrict our discussion to the case where an anisotropic distortion is induced dynamically *via* time-modulated magnetic fields, providing directional control over of topological textures. To this end, we consider a symmetric magnet array ($a = b$) undergoing rigid sinusoidal oscillations along the x-axis. In Fig. 6(a), we show the time-averaged director perturbation $\langle \delta\vec{n} \rangle_t$ induced by the time-averaged magnetic torque $\langle \vec{\Gamma} \rangle_t \propto \left\langle (\vec{n}_0 \cdot \vec{B})\left(\vec{n}_0 \times \vec{B}\right) \right\rangle_t$ acting on $\vec{n}_0$, for different values of the dynamic asymmetry parameter $A_{dyn} = x_{max}/d$, where x_{max} is the oscillation amplitude.

At small values of A_{dyn}, the resulting maps of $\langle \delta\vec{n} \rangle_t$ are topologically equivalent to those discussed in Section 4.2. However, unlike the static approach, the time-averaged method allows for reaching arbitrarily high levels of effective asymmetry, granting access to topological textures that cannot be realized through static magnetic field structuring. We notice that the sign and location of defects both in static and dynamic cases are well correlated with the shape and location of director walls. We use

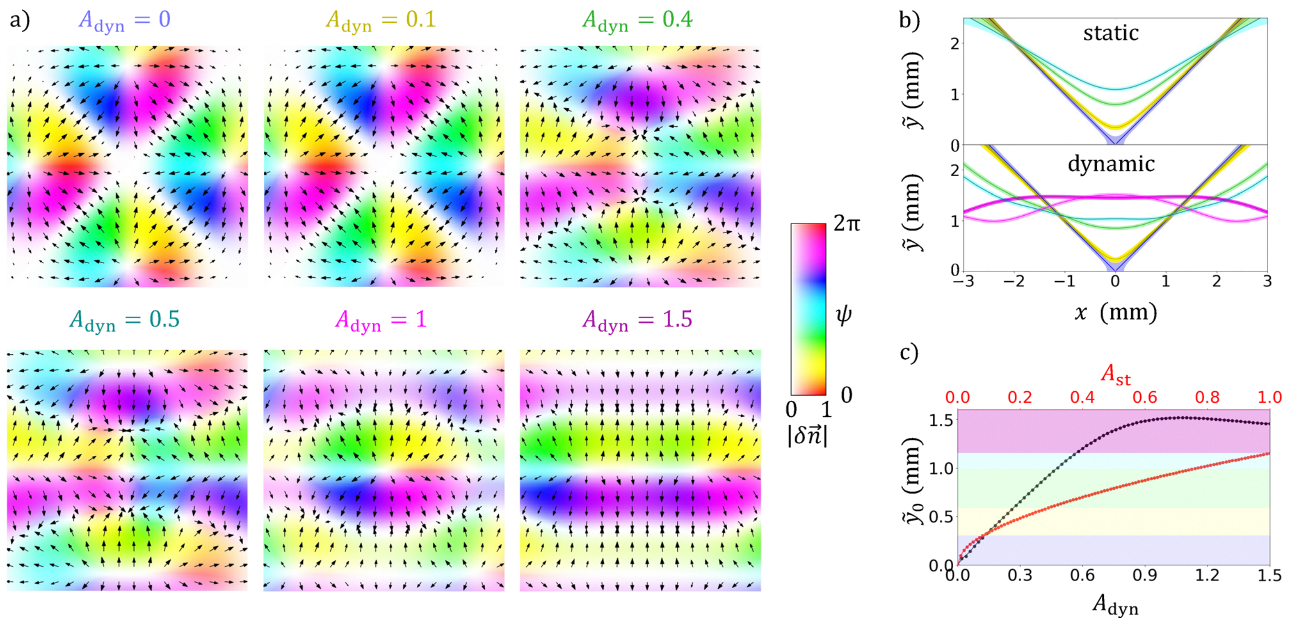

Fig. 6 Numerical simulation of the director seed as a function of the dynamically induced asymmetry. (a) Normalized amplitude (saturation) and azimuth (hue and arrows) of $\langle\delta\vec{n}\rangle_t$ maps in presence of a symmetric magnet array alone oscillating with an amplitude A_{dyn}. (b) Profiles of $|\langle\delta\vec{n}\rangle_t| = 0$ for different values of A_{dyn}. Colors correspond to the values of A_{dyn} indicated in (a). (c) $\tilde{y}_0$ as function of A_{dyn} and A_{st}, representing dynamically and statically induced asymmetry, respectively. Color bands highlight the numerically predicted orientational states from Fig. 5(b) in order to identify the corresponding values of A_{dyn}.

the contours of the walls approximated numerically by zero-amplitude contours of $\delta\vec{n}$ in the (x,y)-plane as a common descriptor to highlight the similarity between the state diagrams in static and dynamic approaches. Specifically, we introduce the curves $\tilde{y}(x)$, defined by the condition $\langle\delta\vec{n}\rangle_t = 0$, and restrict the analysis to the upper half-plane $y > 0$, as illustrated in Fig. 6(b). Our classification of states is based on topology of the central part of the texture, so we can safely reduce the information about the whole contour $\tilde{y}_0(x)$ to the vertical distance $\tilde{y}_0 = \tilde{y}(0)$ from the central axis of the array to the nearest point where the $\delta\vec{n}$ vanishes. In Fig. 6(c), we plot $\tilde{y}_0$ values overlaid with the color bands corresponding to various numerically predicted topological states from the static phase diagram (Fig. 5). This comparison provides a guess for values of A_{dyn} which are likely to reproduce textures previously observed under static conditions based purely on director seed comparison without solving eqn (10) for dynamic case. Notably, we find that regions with $\tilde{y}_0 > 1.15$ mm, which are inaccessible in the static configuration, become reachable for $A_{dyn} > 0.57$. We associate this highly asymmetric regime with the magenta color and denote it as *vii*) in the dynamic phase diagram (Fig. 7). Moreover, the local curvature of $\tilde{y}(x)$ also provides information about the nature of the resulting texture: a curvature reversal typically coincides with a change in the topological charge of the central defect in the director field, as shown in the corresponding $\delta\vec{n}$ maps in Fig. 6(a).

5.2. Controlling umbilic charge *via* time-induced breaking of spatial symmetry

We studied numerically and experimentally how a spatiotemporally structured magnetic field affects the generation of umbilical textures, as summarized in Fig. 7. For small modulation amplitudes $\left(A_{dyn} \lessapprox 0.6\right)$, the sequence of textures resembles the static case. The system evolves from state iii to iv as the central $m = +1$ umbilic shifts off-center, then gives way to the states *v*) and *vi*) with the central $m = -1$ umbilic and two director walls, each containing three or one umbilic around its center, respectively. We relate the transition from the state *v*) to the state *vi*) to a reduction in the local curvature of the Néel wall. For larger amplitudes A_{dyn}, we observe several different states all having a single positive umbilic flanked by two lateral negative umbilics trapped between two convex director walls (states *vii*). For readability of the phase diagram we denote all of them as *vii*) and magenta color, but we numerate them with different numbers. For example, at lower A_{dyn} value we observe the state with two walls each containing single $m = -1$ umbilic which we denote as *vii-1*). As the spatial extent of the system increases with higher A_{dyn} values, the system evolves into the state *vii-2*) characterized by Néel walls containing central $m = +1$ umbilics flanked by two $m = -1$ umbilics.

The transition values of A_{dyn} and observed states differ slightly between experiment and simulation. This difference is clearly noticeable, for example, in the experimentally observed state *v-2*) shown in Fig. 7(c) containing three umbilics on each positively curved wall at $A_{dyn} = 0.83$, whereas the numerically simulated states contained single umbilics on positive curved walls at $0.5 < A_{dyn} < 0.64$ and equivalent β values. We also note that the curvature of the wall remains positive in the experiment up to about $A_{dyn} = 1$ while in the simulation it reverses its sign at lower values about $A_{dyn} = 0.64$. Instead, we observe that both in the experiment and

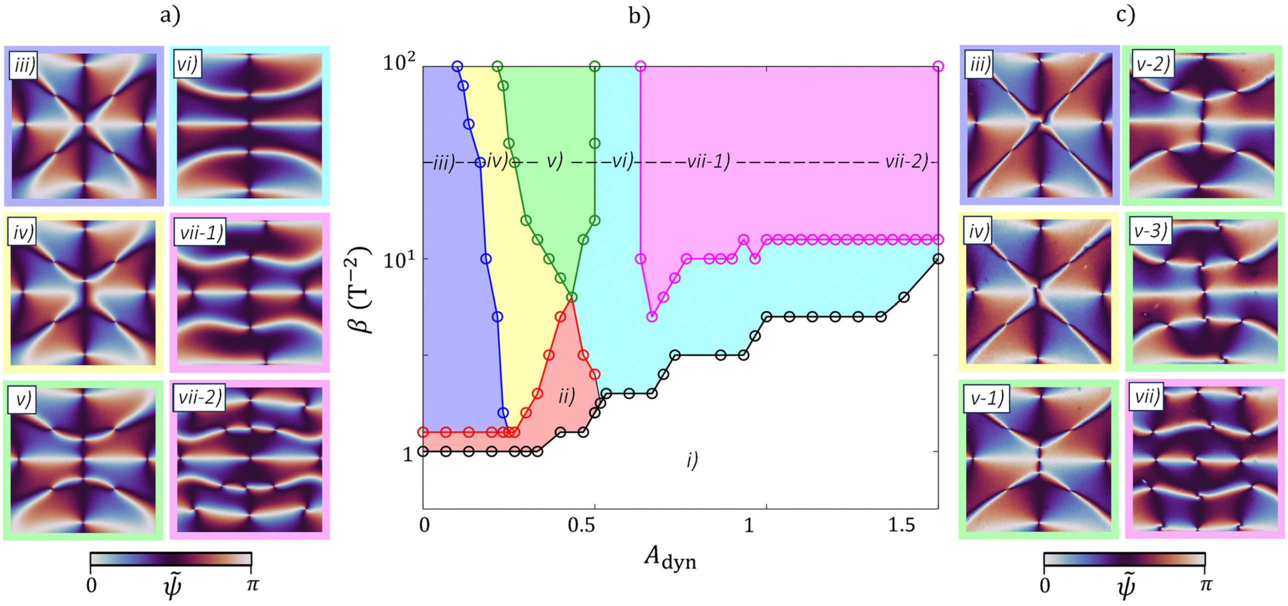

Fig. 7 Numerically simulated and experimentally observed topological textures for dynamic structured magnetic fields provided by the magnet configurations illustrated in Fig. 3. The cyclic color map represents the in-plane director azimuth $\tilde{\psi}$. (a) Numerically simulated (from eqn (10)) textures illustrating unique features of these orientational states: *iii)* An $m = +1$ umbilic trapped in the center of the magnet array at $A_{\mathrm{dyn}} = 0.1$, $\beta = 31.5$ T^{-2}, *iv)* off-centered $m = +1$ umbilic at $A_{\mathrm{dyn}} = 0.23$, $\beta = 31.5$ T^{-2}, *v)* Central $m = -1$ umbilic at $A_{\mathrm{dyn}} = 0.4$, $\beta = 31.5$ T^{-2}, *vi)* central $m = -1$ umbilic and annihilation of umbilic pairs trapped at the wall at $A_{\mathrm{dyn}} = 0.6$, $\beta = 31.5$ T^{-2}, Trapping a central positive umbilic and two side negative umbilics at *vii-1)* $A_{\mathrm{dyn}} = 0.95$, $\beta = 31.5$ T^{-2}, and, *vii-2)* $A_{\mathrm{dyn}} = 1.33$, $\beta = 31.5$ T^{-2}. (b) Diagram of the distinctive states numerically identified by varying A_{dyn} and β. The horizontal dashed line refers to a value of $\beta \approx 30$ T^{-2} that corresponds to our estimation for a typical experiment. (c) Experimentally reconstructed director azimuth maps $\tilde{\psi}(x,y)$ at $A_{\mathrm{dyn}} = 0$, 0.23, 0.5, 0.83, 1.0 and 1.5, respectively. Variations of numerically and experimentally observed states *vii)* and *v)* related to the number of umbilics trapped on the walls and out-centering of $m = +1$ umbilics located under magnets are denoted with numbers 1, 2 and 3. The field of view in each panel is 6 mm × 6 mm.

simulation, $m = +1$ umbilics in the upper and bottom parts of the image get off-centered at similar A_{dyn} values, see states *vii-1*) in Fig. 7(a) and *v-3*) in Fig. 7(c). We relate this difference to the non-sinusoidal nature of the magnet array's oscillation in the experimental setup. In order to bypass technical limitations of the translation stage, its motion profile was defined solely by its amplitude and frequency, and the oscillation frequency was chosen high enough (0.2 Hz for $A_{\mathrm{dyn}} = 1$) to satisfy the overdamped dynamic regime (no variation of the director associated with the movement of the magnets was observed). Despite this discrepancy, both the experiment and the simulation confirm that the periodic translation of a given magnetic array in the overdamped regime can seed a variety of umbilic textures. We also emphasize the key role played by the local curvature of the magnetic landscape in determining the sign of the seeded umbilics.

5.3. Controlling umbilic charge *via* time-induced restoration of spatial symmetry

Here, we address the reverse problem: restoring axial symmetry in the seeded director field *via* time modulation. To this end, we consider an asymmetric array of permanent magnets and recover axial symmetry by rotating the array at constant speed around its central axis. To illustrate this, we compute the time-averaged director perturbation from eqn (1) as the sum of ϕ-averaged radial and polar contributions:

$$\langle \delta\vec{n}\rangle_t = \langle \delta n_\rho\rangle_t \vec{e}_\rho + \langle \delta n_\phi\rangle_t \vec{e}_\phi = \frac{1}{2\pi}\int_{-\pi}^{\pi}\left(\delta n_\rho \vec{e}_\rho + \delta n_\phi \vec{e}_\phi\right)\mathrm{d}\phi, \qquad (11)$$

taking into account the mirror symmetry of the magnetic field provided by the magnet configurations illustrated in Fig. 3(a):

$$B_\rho\vec{e}_\rho + B_\phi\vec{e}_\phi + B_z\vec{e}_z \xrightarrow{\phi\to-\phi} B_\rho\vec{e}_\rho - B_\phi\vec{e}_\phi + B_z\vec{e}_z. \qquad (12)$$

Here, the subscripts ρ, ϕ, and the vectors $\vec{e}_\rho$ and $\vec{e}_\phi$ refer to the radial and angular polar coordinates and their unit vectors, respectively. We notice that the effect of the azimuthal component of the static magnetic seed averages out upon the integration, leaving only the radial component at work. As a result, the director textures resemble those produced by a symmetric disk or a ring magnet.[17] Experimentally, we implement this approach by using an asymmetric ($a \neq b$) array of four cube magnets (8 mm side) with alternating polarity, assembled with a static asymmetry $A_{\mathrm{st}} = 0.34$ (see Fig. 8). The array is rotated in the (x,y) plane around its center using a motorized rotation stage at a frequency $f = 0.5$ Hz, which is high enough to ensure the overdamped dynamics (no variation of the director associated with the movement of the magnets was observed). Moreover, to distinguish $m = +1$ and $m = -1$ umbilics directly from the cross-polarized images, we rotate the polarizer-analyzer pair to +15°. As shown Fig. 8, the Maltese cross associated with an $m = +1$ umbilic follows this rotation, while

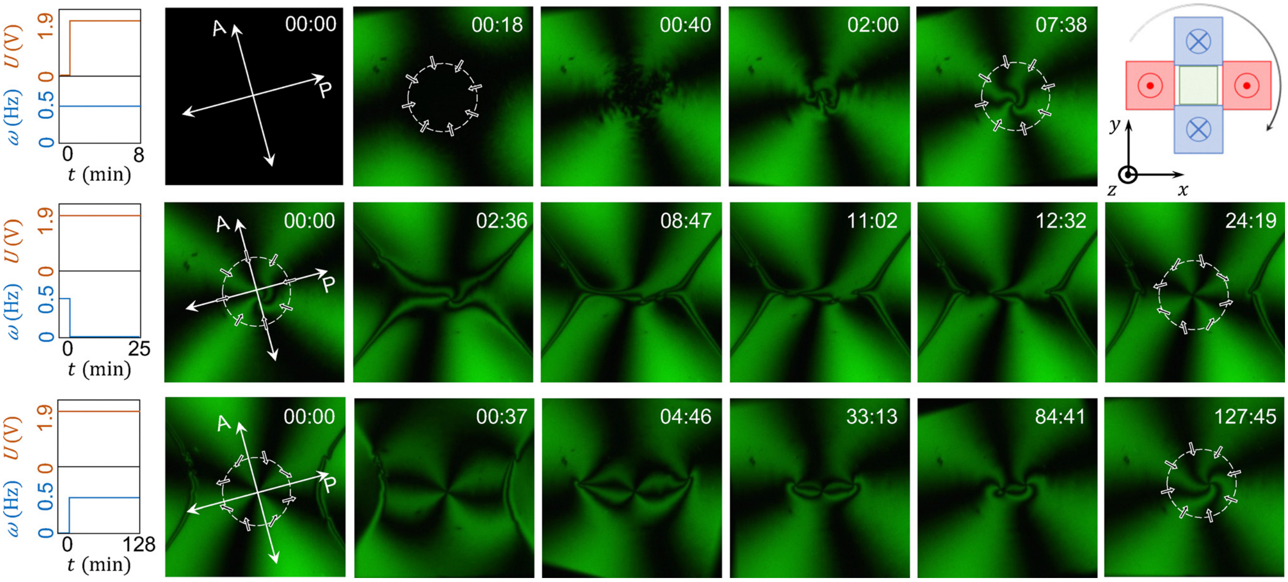

Fig. 8 Cross polarized microscope images of nematic sample under the action of uniform AC electric field and rotated magnetic array made of four 8 mm side cubes, $A_{\mathrm{st}} \approx 0.4$. Top row: morphogenesis of the texture in the first scenario. Middle row: umbilics triplet restoration after stopping the magnet array rotation. Bottom row: morphogenesis of the texture in the second scenario. The field of view in each image is 6.3 mm × 6.3 mm wide (indicated as green rectangle in the center of the sketch of the magnet array), the time stamp in mm:ss is indicated in each image.

the one corresponding to an $m = -1$ umbilic rotates in the opposite direction.

We consider two scenarios. In the first (top row of Fig. 8), the magnet array with static asymmetry A_{st} corresponding to the state ν) in Fig. 5 is set into rotation and brought close to the initially unperturbed sample. Upon application of an electric field, the resulting director texture exhibits a central $m = +1$ umbilic near the rotation axis, similar to the texture induced by a uniform ring magnet.[20] This demonstrates that the rotation of an asymmetric array generates an effective seed with radial symmetry, enabling the generation of a single $m = +1$ umbilic with a large clear aperture.

When the rotation is stopped, the system reverts to a triplet of umbilics (middle row of Fig. 8) through a process that begins with the outer director field adopting a configuration similar to that of an $m = -1$ umbilic. This is evidenced by the appearance of an outer Maltese cross oriented at $-15°$ relative to the x- and y-axes, and by the emergence of a pair of Néel walls whose orientation is set by the final position of the magnet array as it halts. The subsequent evolution of this texture depends on the value of A_{st}. For large enough A_{st} from region ν) in Fig. 5, Néel walls approach and eventually cross each other creating two new pairs of umbilics. One of these pairs of umbilics annihilate each other, and three remaining umbilics form the static triplet configuration (state ν) in Fig. 5. For lower A_{st} values from the ν), a bistability can be observed, as illustrated numerically in Fig. 9: the recreated Néel walls do not cross as the magnet array halts and the texture relaxes to the state $i\nu$) with an off-centered $m = +1$ umbilic.

In the second scenario (bottom row in Fig. 8), the static asymmetric magnet array is first brought close to the unperturbed sample, after which an electric field is applied, leading to the formation of a triplet of umbilics. Once the steady-state texture is established, the magnet array is set into rotation. The outer director field progressively evolves towards a configuration with positive topological charge, as indicated by the appearance of an outer Maltese cross oriented at $+15°$ relative to the x- and y-axes (observed at t = 4 min 46 s). This evolution is accompanied by a reduction in the distance between the central $m = -1$ umbilic and its two neighboring $m = +1$ umbilics, leading to the annihilation of the nearest pair. The remaining $m = +1$ umbilic then drifts toward the center of the array, similar to the behavior observed under a static ring magnet with uniform magnetization.[20] The results of numerical simulations featuring texture transformations from these two scenarios are provided in the SI Videos.

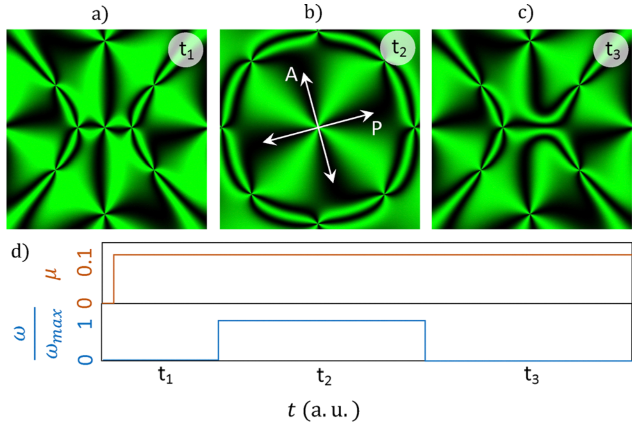

Fig. 9 Numerical equivalent of cross polarized images of simulated topological textures for structured magnetic fields provided by the magnet configuration illustrated in Fig. 8 with $A_{\mathrm{st}} \approx 0.3$, (a) before, (b) during and (c) after the rotation. The field of view in each panel is 9 mm × 9 mm.

6. Conclusion

In this work, we investigated, both numerically and experimentally, the controlled generation of topological textures in thin films of nematic liquid crystals using the combined action of spatiotemporally structured magnetic fields and uniform quasistatic electric fields. Starting from the Frank–Oseen free energy, we derived a two-dimensional amplitude equation describing the evolution of the director field under spatial and temporal modulations of the magnetic components B_z and $\vec{B}_\perp$. This quantitative framework was complemented by a qualitative approach based solely on the orientational response to the magnetic torque density, providing intuitive insight into the initial seeding of orientational textures that later evolve under the action of the electric field.

Our results show that a wide variety of umbilic textures can be generated using simple arrays of four permanent magnets, whose symmetry dictates the diversity of accessible orientational states. In particular, we demonstrate control over the sign of the central topological charge. The method enables the formation of textures with a clear aperture of several millimeters around the central umbilic, which is of direct relevance for photonic applications.[20,37]

We further explored the role of temporal modulation of the magnetic field. Rectilinear oscillation of the magnet array allows one to overcome spatial constraints of static configurations, while rotational modulation introduces additional degrees of control. In this regime, we demonstrated switching between textures with central umbilics of opposite topological charge, thus offering routes for deterministic generation of topological defects beyond standard quench-based approaches.

Beyond the specific context of nematic liquid crystals, our strategy provides a versatile platform for spatiotemporal structuring in other magnetically responsive systems, including colloidal, active, and biological media. This opens new directions for the design and control of field-responsive materials with tailored topological properties.

Author contributions

N. Kravets: conceptualization (equal), experiment (lead), writing – original draft (lead), writing – review and editing (equal). G. Gonzalez-Cortes: conceptualization (supporting), numerical simulation (lead); writing – original draft (supporting), writing – review and editing (equal), E. Brasselet: conceptualization (equal); experiment (supporting); writing – review and editing (equal).

Conflicts of interest

There are no conflicts to declare.

Data availability

The numerically generated videos supporting this article have been included as part of the supplementary information (SI). Supplementary information: videos of topological texture evolution under the action of magnetic field of rotating array. See DOI: **https://doi.org/10.1039/d5sm00671f**.

The numerical data and the experimental data are available at reasonable request from the authors.

Acknowledgements

This research was partially financed by French National Research Agency (ANR) as part of the project ANR-23-CE06-0013-01. Gregorio Gonzalez-Cortes thanks for the European Union's Horizon research and innovation program Marie Sklodowska-Curie grant OPS-CLC agreement No 101067273.

Notes and references

1 P. de Gennes and J. Prost, *The Physics of Liquid Crystals*, Clarendon Press, 1993.
2 M. O. Katanaev, *Phys.-Usp.*, 2005, **48**, 675.
3 R. B. Hoyle, *Pattern formation: an introduction to methods*, Cambridge University Press, 2006.
4 A. Rapini, *J. Phys.*, 1973, **34**, 629–633.
5 V. Fréedericksz and V. Zolina, *Trans. Faraday Soc.*, 1933, **29**, 919–930.
6 I. Dierking, O. Marshall, J. Wright and N. Bulleid, *Phys. Rev. E: Stat., Nonlinear, Soft Matter Phys.*, 2005, **71**, 061709.
7 P. Pieranski, E. Dubois-Violette and E. Guyon, *Phys. Rev. Lett.*, 1973, **30**, 736.
8 V. Chigrinov, T. Korkishko, M. Barnik and A. Trufanov, *Mol. Cryst. Liq. Cryst.*, 1985, **129**, 285–300.
9 Y. Sasaki, V. Jampani, C. Tanaka, N. Sakurai, S. Sakane, K. V. Le, F. Araoka and H. Orihara, *Nat. Commun.*, 2016, **7**, 13238.
10 M. G. Clerc, M. Kowalczyk and V. Zambra, *Sci. Rep.*, 2020, **10**, 19324.
11 E. Brasselet, *Opt. Lett.*, 2009, **34**, 3229–3231.
12 R. Barboza, U. Bortolozzo, G. Assanto, E. Vidal-Henriquez, M. G. Clerc and S. Residori, *Phys. Rev. Lett.*, 2012, **109**, 143901.
13 I. A. Budagovsky, A. S. Zolot'ko, M. P. Smayev and S. A. Shvetsov, *Bull. Lebedev Phys. Inst.*, 2015, **42**, 319–322.
14 C. Loussert, K. Kushnir and E. Brasselet, *Appl. Phys. Lett.*, 2014, **105**, 121108.
15 R. You, Y.-S. Choi, M. J. Shin, M.-K. Seo and D. K. Yoon, *Adv. Mater. Technol.*, 2019, **4**, 1900454.
16 M. Kim and F. Serra, *Adv. Opt. Mater.*, 2020, **8**, 1900991.
17 F. Brochard, L. Léger and R. B. Meyer, *J. Phys. Colloques*, 1975, **36**, C1-209–C1-213.
18 J. M. Gilli, M. Morabito and T. Frisch, *J. Phys. II France*, 1994, **4**, 319–331.
19 P. Pieranski, B. Yang, L. J. Burtz, A. Camu and F. Simonetti, *Liq. Cryst.*, 2013, **40**, 1593–1608.
20 E. Brasselet, *Phys. Rev. Lett.*, 2018, **121**, 033901.
21 E. Calisto, M. G. Clerc and V. Zambra, *Phys. Rev. Res.*, 2020, **2**, 042026.
22 L. Migara and J.-K. Song, *NPG Asia Mater.*, 2018, **10**, e459.
23 R. M. Erb, J. J. Martin, R. Soheilian, C. Pan and J. R. Barber, *Adv. Funct. Mater.*, 2016, **26**, 3859–3880.

24 P. Guillamat, J. Ignés-Mullol and F. Sagués, *Proc. Natl. Acad. Sci. U. S. A.*, 2016, **113**, 5498–5502.

25 Y. Ishii, Y. Zhou, K. He, Y. Takanishi, J. Yamamoto, J. de Pablo and T. Lopez-Leon, *Soft Matter*, 2020, **16**, 8169–8178.

26 S. Chandrasekhar, *Liquid Crystals*, Cambridge University Press, 1992.

27 R. Barboza, U. Bortolozzo, M. G. Clerc, S. Residori and E. Vidal-Henriquez, *Phil. Trans. R. Soc. A*, 2014, **372**, 20140019.

28 T. Nagaya, H. Hotta and H. Oriharaand Yoshihiro Ishibashi, *J. Phys. Soc. Jpn*, 1992, **61**, 3511–3517.

29 I. Chuang, B. Yurke, A. N. Pargellis and N. Turok, *Phys. Rev. E: Stat. Phys., Plasmas, Fluids, Relat. Interdiscip. Top.*, 1993, **47**, 3343.

30 I. Dierking, M. Ravnik, E. Lark, J. Healey, G. Alexander and J. Yeomans, *Phys. Rev. E: Stat., Nonlinear, Soft Matter Phys.*, 2012, **85**, 021703.

31 T. Frisch, S. Rica, P. Coullet and J. M. Gilli, *Phys. Rev. Lett.*, 1994, **72**, 1471–1474.

32 T. Frisch, *Phys. D*, 1995, **84**, 601–614.

33 N. Derby and S. Olbert, *Am. J. Phys.*, 2010, **78**, 229–235.

34 A. Caciagli, R. J. Baars, A. P. Philipse and B. W. Kuipers, *J. Magn. Magn. Mater.*, 2018, **456**, 423–432.

35 M. Ortner and L. G. C. Bandeira, *SoftwareX*, 2020, **11**, 100466.

36 E. Dubois-Violette, P. De Gennes and O. Parodi, *J. Phys.*, 1971, **32**, 305–317.

37 A. Aleksanyan and E. Brasselet, *Opt. Lett.*, 2016, **41**, 5234–5237.